JOURNAL OF SPACECRAFT AND ROCKETS
Vol. 34, No. 4, July–August 1997

High-Enthalpy Aerothermodynamics of a Mars Entry Vehicle Part 2: Computational Results

Brian R. Hollis* and John N. Perkins†
North Carolina State University, Raleigh, North Carolina 27695-7910

Numerical solutions for hypersonic flows of carbon dioxide and air around a 70-deg sphere–cone Mars entry vehicle configuration were computed using a laminar, axisymmetric, nonequilibrium Navier–Stokes solver with freestream flow conditions equivalent to those of aerothermodynamic tests conducted in a high-enthalpy impulse facility. The wake flowfield computations were found to be much more sensitive to both grid resolution and grid adaptation than the forebody results. The wake computations showed the existence of a region of separated, steady, recirculating flow behind the vehicle. Whereas the rapid expansion of the flow around the corner of the vehicle resulted in a wake that was mostly frozen both chemically and vibrationally, the degree of flow expansion was not great enough to produce noncontinuum flow behavior. Comparisons between computational and experimental surface heating distributions were within the estimated experimental uncertainty for both cases except around the forebody stagnation point and the free-shear-layer reattachment point for the air case and within a small portion of the wake recirculation vortex for the carbon dioxide case.

Nomenclature

h	= enthalpy, J/kg
Kn	= Knudsen number
M	= Mach number
p	= pressure, N/m^2
q	= heat transfer rate, W/m^2
R	= radius, m
Re	= Reynolds number
S	= distance along model surface, m
T	= temperature, K
U_∞	= freestream velocity, m/s
Y_s	= species mass fraction
λ_{MFP}	= mean free path, m
ρ	= density, kg/m^3

Subscripts

0	= total
1	= freestream
2	= post-normal shock

Introduction

In recent years, NASA has embarked on a long-term exploration initiative[1] in which unmanned orbiters and landers will be employed to gather scientific data on the planet Mars. This initiative has produced renewed interest in blunt-body entry vehicle and aerobrake configurations such as the 70-deg sphere–cone geometry of the Mars Pathfinder (formerly known as MESUR) spacecraft.[2] This interest has led to a number of computational and experimental studies of blunt-body flows[3–14] in perfect-gas, high-enthalpy, and rarefied environments.

This present study contributes to the growing database on blunt-body flows through the presentation of comparisons between blunt-body heat transfer rates measured in a high-enthalpy impulse facility and those obtained from flowfield solutions computed using a nonequilibrium Navier–Stokes solver. These experiments and computations were conducted in test gas environments (CO_2 and N_2–O_2) representative of the atmospheres of Mars and Earth, and encompassed both the forebody and wake (that is, the afterbody and model sting) regions of the flow. The experimental data from this study are presented in Part 1 (Ref. 15) of this work, and the computational results are presented here.

The subject of this work was a 70-deg sphere–cone configuration derived from the geometry of the Mars Pathfinder spacecraft. This sphere–cone geometry is shown in Fig. 1; the locations of control points on the model and sting in terms of nondimensional distance from the forebody stagnation point, S/R_b, are also shown in Fig. 1. The radius of the sphere–cone forebody was 2.54 cm (1 in.). The forebody had a nose-radius/forebody-radius ratio of 0.5 and a corner-radius/forebody-radius ratio of 0.05. This configuration also had a 40-deg cone-frustum afterbody, which represented the payload section of the vehicle. The cone-frustum angle was altered from that of Mars Pathfinder (49.5 deg) to accommodate the sting that was used to support the model in the test facility. This change was considered to be acceptable, as the presence of the sting would alter the wake flowfield in any event. The sting was fitted to a 45-deg cone strut adapter. The adapter was mated to the sting at a point 4.6 forebody base radii downstream from the frustum, which was a sufficient distance to ensure that boundary-layer separation induced by the shock at the adapter would not influence the near-wake region of interest directly behind the model.

Whereas this research encompassed both the forebody and wake regions of the sphere–cone configuration, emphasis was placed on measurements and computations for the wake of the configuration. The important features of a blunt-body wake flowfield (Fig. 2) are a free shear layer formed by the separation of the forebody boundary layer at or around the corner of the vehicle, a recirculating flow region in the wake of the vehicle, a free-shear-layer impingement point on the sting (or a neck region in the case of actual spacecraft, which would not have a sting), and a recompression shock formed as the free shear layer is turned back into the direction of the freestream. These features define the aerothermodynamic environment of the wake, and their behavior influences the design of an aerobrake or entry vehicle. Thermal protection shielding on the payload of the vehicle must be sufficient to withstand the aerothermodynamic loads imposed upon it, and the size and placement of the payload must be such that the wake free shear layer does not impinge upon it, or a localized region of high heating will be produced.

Computational Method

Numerical solutions of the Navier–Stokes equations[16] for the flow around the vehicle geometry were computed using the NEQ2D[17] code, an implicit, laminar, two-dimensional/axisymmetric Navier–Stokes solver. Solution of the governing equation set is accomplished in NEQ2D through the use of the line Gauss–Seidel

Received Aug. 15, 1996; revision received March 2, 1997; accepted for publication March 15, 1997.

*Graduate Researcher, Department of Mechanical and Aerospace Engineering. Member AIAA.

†Professor, Department of Mechanical and Aerospace Engineering. Associate Fellow AIAA.

Table 1 HYPULSE test conditions

Test gas	ρ_1, kg/m^3	U_1, m/s	T_1, K	P_1, Pa	$h_0 - h_{289K}$, MJ/kg	$P_{0,2}$, MPa	$T_{0,2}$, K
CO_2	0.00579	4772	1088	1187	12.25	0.130	3700
	±3.1%	±1.1%	±8.7%	±10.8%	±2.1%	±1.8%	±0.9%
Air	0.00571	5162	1113	1824	14.18	0.147	6027
	±1.8%	±0.9%	±9.3%	±9.9%	±1.4%	±1.3%	±0.8%

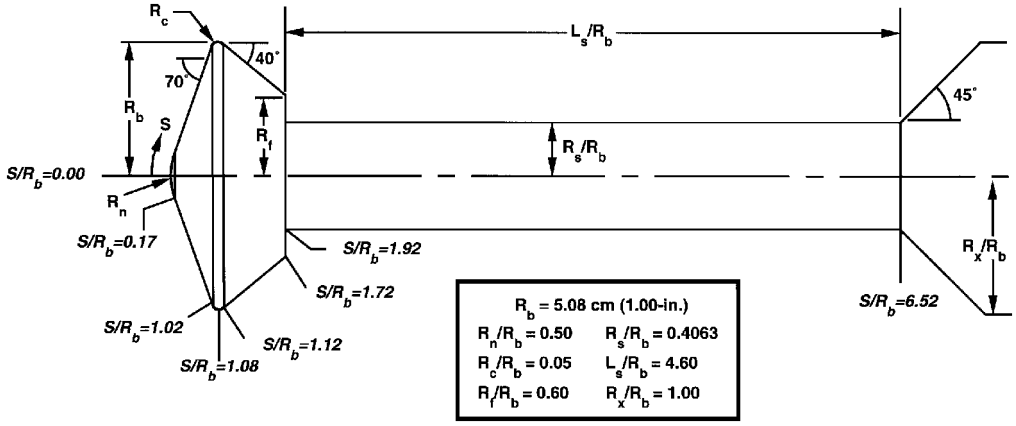

Fig. 1 Model and sting geometry.

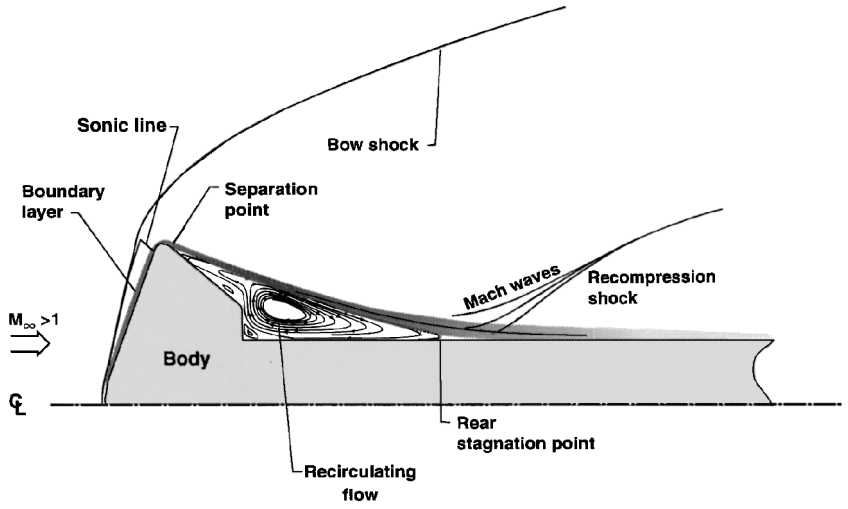

Fig. 2 Blunt-body wake flow structure.

technique.[18] Inviscid fluxes are computed through a modified Steger–Warming[18] flux-splitting technique, which minimizes numerical dissipation in boundary layers. In high-pressure gradient regions, such as near the bow shock, this flux-splitting method reverts to the original Steger–Warming technique to maintain numerical stability. Viscous fluxes are computed through second-order central differences. Vibrational nonequilibrium is represented through the two-temperature model of Park.[19] Nonionizing thermochemical models in NEQ2D for Earth[19] (N_2–O_2–NO–N–O) and Mars[20] (CO_2–CO–N_2–O_2–NO–C–N–O) atmospheres were employed in this study.

Solutions were computed for conditions equivalent to those at which Mars entry vehicle models were tested in the HYPULSE Expansion Tube, as detailed in Part 1 (Ref. 15) of this work. Freestream flow properties for the test cases are listed in Table 1, and the nondimensional simulation parameters are given in Table 2. The freestream species mass fractions were taken to be $Y_{CO_2} = 1.00$ for the CO_2 case and $Y_{N_2} = 0.76533$ and $Y_{O_2} = 0.23467$ for the air case. Because of the extremely short data acquisition period during a HYPULSE test (125–150 μs), the model surface temperatures remained essentially independent of the freestream total temperature, which drives the aerodynamic heating of the model. Therefore, wall temperatures were set to a uniform value of 300 K. Owing to the low surface temperature and the use of Macor® (Corning, Inc.), a ceramic material, in the construction of the test models, a noncatalytic wall boundary condition was specified.

Eigenvalue limiters are incorporated in the NEQ2D code to maintain stability around stagnation points. In Ref. 10, tuning of these eigenvalues to fit computational fluid dynamics (CFD) results to experimental data is cited as producing case-dependent results with NEQ2D. In that reference, this difficulty was avoided by modifying the code to remove the eigenvalue limiters. In the present study, the eigenvalue dependence was minimized by using the lowest possible eigenvalue limiter values (where zero values correspond to the true physics of the problem) for which stability could be maintained. For the normal flux representation, limiters on the eigenvalues were set to near-zero values ($<10^{-3}$); for the streamwise flux representation, values between 0.2 and 0.6 were employed, depending on the case. Limiter values were kept low enough that the computational solutions were independent of them everywhere except around stagnation points. From the behavioral trend observed on decreasing the limiters, it was estimated that the minimum limiter values required for stability caused an underprediction of ≈5% or less of surface heating rates in the regions around stagnation points.

Table 2 HYPULSE simulation parameters

Test gas	M_1	$Re_{1,d}$	Kn_1	ρ_2/ρ_1
CO_2	9.71	3.35×10^4	0.00037	18.98
Air	7.93	3.39×10^4	0.00028	10.98

Grid Generation, Adaptation, and Refinement

The structure of the computational grids was found to have a large influence on the wake flowfield computations. Therefore a grid resolution study was conducted, and grid manipulation techniques were employed to adapt the grid to the features of the flowfields.

Initial grids for the two test cases were constructed using an elliptical grid generation algorithm. The grids were separated into forebody and wake zones along the normal grid line from the outermost point on the forebody corner. Flowfield distributions at the supersonic outflow boundaries of the forebody grids were used as starting conditions for solutions on the wake grids. This grid separation optimized the computational process because solutions on the wake grids converged slower than on the forebody grids and also required lower Courant–Friedrichs–Lewy (CFL) numbers to retain stability. After converged solutions on the separated grids were obtained, they were rejoined, and the computations were continued. The final solutions computed on the unified grids were identical to those on the separated grids, which demonstrated that the supersonic extrapolation boundary between the two grids did not affect the final solutions.

After converged solutions were obtained on the initial grids, the grids were adapted to the flowfield characteristics through a two-step process. The first step was an algebraic grid adaptation along grid lines normal to the wall boundary.[21] The purpose of this step was to align the streamwise grid lines with the bow shock and to cluster points within the wall boundary layer. The second step was to adapt the grid to the wake free shear layer and recirculation vortex using the Volume Grid Manipulator (VGM) code.[22] The purpose of this step was to minimize grid-produced artificial dissipation in the viscous wake free shear layer and recirculation vortex.

In the first step, in which the grid points were clustered near the wall, the height of the first cell from the wall was initially set to a cell Reynolds number (based on local sonic speed) of the order of 1 for all wall cells. However, it was found that the extremely large differences in density between the forebody and wake flows resulted in unreasonably large cell growth in the separated flow region of the wake when all wall cells were fixed at a uniform Reynolds number. Instead, cell heights were set to a uniform value for all wall cells. Test computations were performed with wall cell heights between 10^{-7} and 10^{-5} m, and it was found that the wall heating values were nearly invariant for cell heights ($\sim 10^{-6}$ m) that produced cell Reynolds numbers of the order of 10 or below. It was also observed that obtaining the necessary small boundary-layer cell sizes required for viscous computations through this algebraic adaptation instead of through the initial elliptic grid generation process eliminated most of the grid-line skewing common to elliptic grid generation schemes near viscous wall boundaries. This greatly reduced the numerical difficulties around axisymmetric stagnation points that are typically associated with upwind CFD codes.

After the first adaptation step was completed and new solutions were computed on the adapted grids, the VGM code was employed to further adapt the grids to the features of the wake flow. As was shown in Fig. 2, wake flows are characterized by a free shear layer and a recirculation vortex, both of which are regions of strong viscous gradients. High grid-point density is needed in these regions to resolve these gradients, and it is also necessary to align the grid with the free shear layer to minimize numerical dissipation caused by skewness of the grids with respect to the flow direction. To fulfill these requirements, the VGM code was used to cluster normal grid points within the free shear layer and recirculation vortex and to align the streamwise grid lines with the free shear layer. The final structure of the grids after adaptation with VGM is shown in Fig. 3 for the CO_2 case and in Fig. 4 for the air case.

In the course of this grid-resolution/grid-adaptation study, solutions were first computed on unadapted grids with 125 streamwise by 90 normal grid points for both cases. These baseline grids were adapted through the process described, and new solutions were then

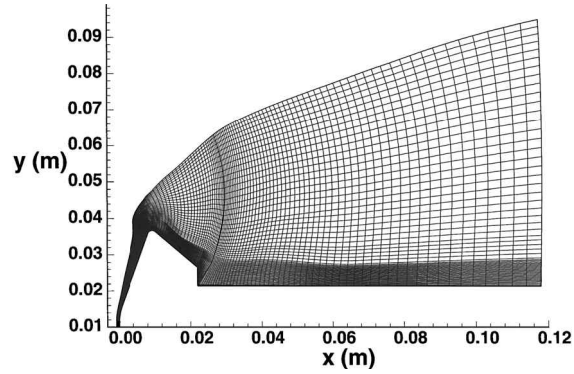

Fig. 3 Free-shear-layer-adapted (125 × 180) point grid for CO_2.

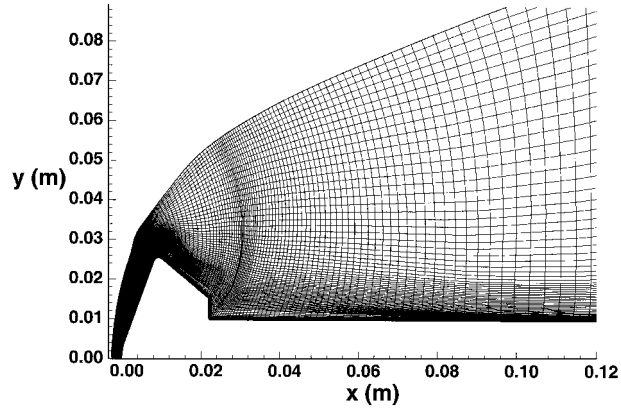

Fig. 4 Free-shear-layer-adapted (125 × 180) point grid for air.

computed. A grid resolution study was then conducted by constructing grids with (125 × 45) and (125 × 180) points from the adapted (125 × 90) point grids. Computed surface heating distributions were used as the basis for evaluating the effects of these grid manipulations. These surface heating distributions are presented in Figs. 5a and 5b for the CO_2 case and in Figs. 6a and 6b for the air case. In general, the wake heating distributions were very sensitive to both grid resolution and grid alignment. Forebody heating was much less sensitive to grid resolution than wake heating, and, of course, was not affected by adaptation of the wake grid.

As shown in Figs. 5a and 6a, forebody heating changed by less than 10% between the (125 × 45) and (125 × 90) point grids, except around the stagnation point for the air case. Heating rates changed by less than 3% between the (125 × 90) and (125 × 180) point grids, and so the (125 × 180) point grid forebody solutions are considered to have reached grid convergence.

The viscous region of the wake (the free shear layer and recirculation vortex) is much larger than the viscous region of the forebody (the attached boundary layer), and so the wake heating distributions proved to be much more sensitive to grid resolution. As shown in Figs. 5b and 6b, heating rates within the wake vortex (S/R_b values of ≈1.0–3.5) decreased sharply with each increase in grid resolution. The heating rates within the wake vortex dropped by ≈15% between the (125 × 45) and (125 × 90) point grids for CO_2 and by ≈10% for air. Between the (125 × 90) and (125 × 180) point grids, the heating rates dropped by ≈10% for CO_2 and by ≈5% for air. The better adaptation results obtained for the air case are not attributed to any physical differences between the two cases but are due to the fact the CO_2 computations were performed first, and the experience gained in performing the adaptations was applied to the air case. Heating rates on for the sting boundary layer downstream of the reattachment point (after $S/R_b \approx 3.5$) were much less sensitive than those in the separated-flow region of the recirculation vortex. Also, as shown in Figs. 5b and 6b, the heating distributions on the original unadapted (125 × 90) point grids compared poorly to even the low-resolution (125 × 45) point adapted-grid results, both within the wake vortex and downstream of reattachment on the sting.

Based on the results of this study, it is estimated that the surface heating rates within the wake vortex were overpredicted by

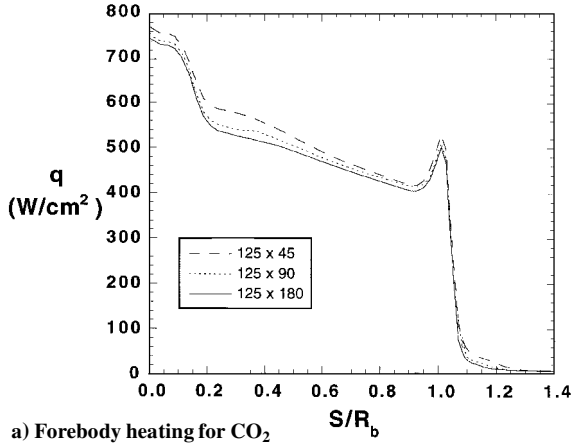

a) Forebody heating for CO_2

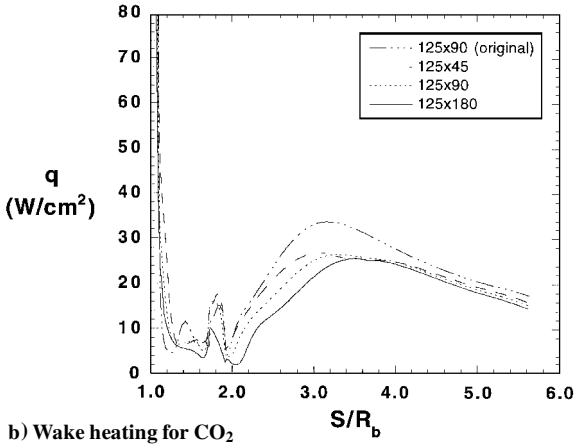

b) Wake heating for CO_2

Fig. 5 Effects of grid resolution and adaptation.

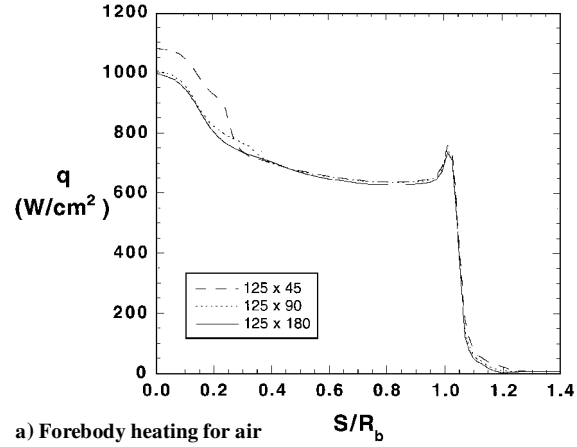

a) Forebody heating for air

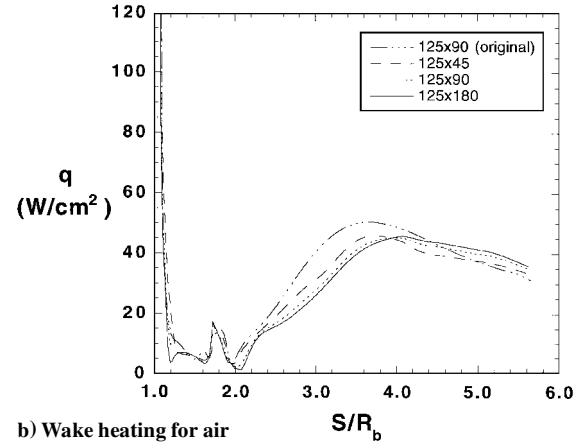

b) Wake heating for air

Fig. 6 Effects of grid resolution and adaptation.

at least 10% for CO_2 and by at least 5% for air, whereas overprediction of the heating downstream of reattachment was negligible. Further increases in grid resolution were cost-prohibitive because of the computational overhead of the nonequilibrium thermochemical models employed for these cases.

From these results it can be seen that wake grid adaptation and grid resolution have a large influence on the wake flowfield. Both adapting the grid and increasing the grid-point resolution tend to minimize grid-produced artificial dissipation. The reduction of artificial dissipation then leads to a growth in the size of the viscous wake vortex, which produces a downstream movement of the peak sting heating point and a decrease in the surface heating within the vortex.

This sensitivity of the wake heating to the grid structure could lead to misinterpretation of comparisons between computations and experimental data for cases in which the wake free shear layer becomes turbulent. While the measured ratio of peak sting heating to forebody stagnation-point heating for a turbulent wake[3–6,13] may be more than double that for a laminar wake, laminar computations on unadapted grids with insufficient grid resolution may greatly overpredict the wake heating distributions and locate the peak heating and free-shear-layer reattachment points further upstream than they should be, and thus appear similar to the turbulent data. As it is not always possible to determine the state of the wake free shear layer from experimental evidence, and no reliable criteria exist (see Ref. 23 for an approximate analysis) for predicting when transition will occur in a hypersonic wake, comparisons such as these may lead to wake flow data being misinterpreted as laminar when they are, in fact, turbulent.

An unpublished preliminary comparison of experimental data with unadapted wake computations was one of the reasons for the assumption that perfect-gas test data in Ref. 3 were laminar, when they have since been concluded to be turbulent.[4] Although other factors such as test flow quality, wake flow establishment during the experiment, continuum flow breakdown, and unsteady wake behavior should also be considered, the wake grid structure may also be the reason for the discrepancies between experiment and computation noted in Refs. 10 and 13. In both of those cases, the surface heating on the sting within the wake vortex was overpredicted, and the predicted location of the peak heating point on the sting was located upstream of the measured location, which is behavior characteristic of computational solutions on nonoptimal grids.

Computational Results

Stagnation-point normalized surface heating and pressure distributions for the two cases are given in Fig. 7a for the forebody and in Fig. 7b for the afterbody and sting. The normalized forebody distributions for these two cases are similar, although the higher shock density ratio (Table 2) in the CO_2 case (which is thus closer to Newtonian flow) produces a flatter pressure distribution and a more linear heating decrease in the direction of the corner. The surface quantities drop by over two orders of magnitude as the flow expands around the forebody corner, and the small local maxima in the distributions around $S/R_b = 1.7$ correspond to the afterbody corners. On the sting, the maximum pressure and heating occurs between S/R_b values of 3.5–4.5, which is slightly downstream of the free-shear-layer reattachment point. The peak sting heating values are only on the order of 3–4% of the forebody stagnation-point heating, which is consistent with laminar flow results.[11–14]

The overall flowfield structure is illustrated by the Mach number contour plots in Figs. 8a and 8b for the two cases. The forebody flow is entirely subsonic up to the corner tangency point where the sonic line is located. Rapid expansion around the forebody corner produces high Mach numbers in the outer inviscid region of the wake and causes nearly complete freezing of the chemical and vibrational processes in the wake (Figs. 9a and 9b). After the forebody corner, the boundary layer separates from the afterbody of the vehicle to form a free shear layer, which reattaches to the sting downstream of the base of the vehicle. The flow within the

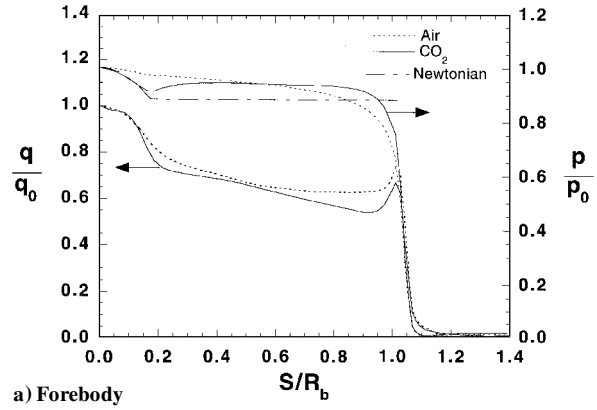

a) Forebody

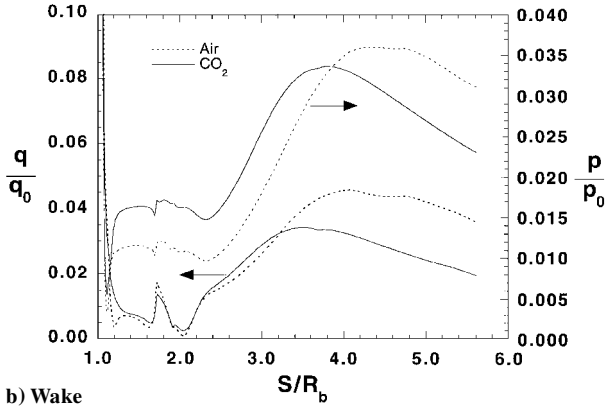

b) Wake

Fig. 7 Normalized surface heating and pressure distributions.

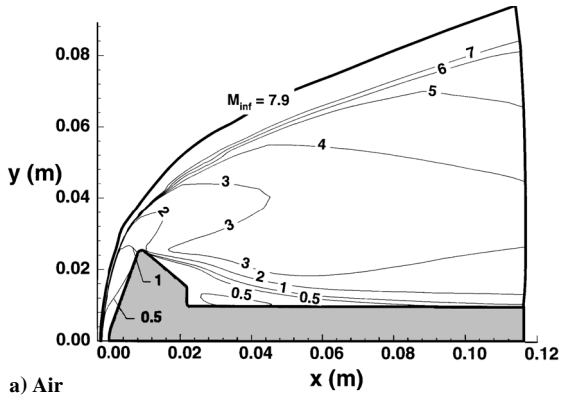

a) Air

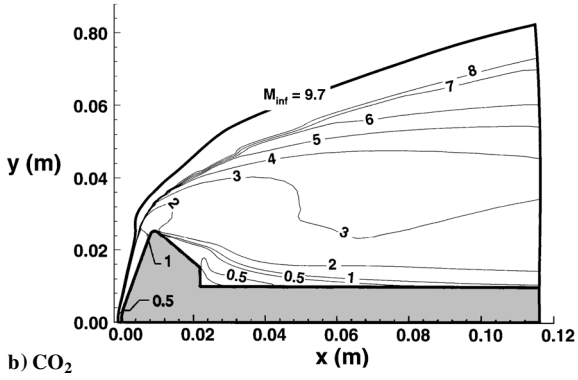

b) CO_2

Fig. 8 Mach number contour plots.

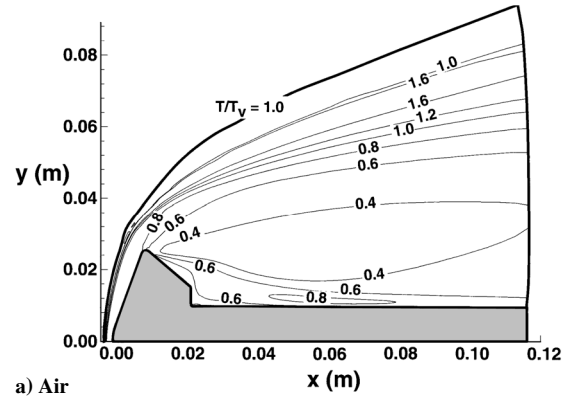

a) Air

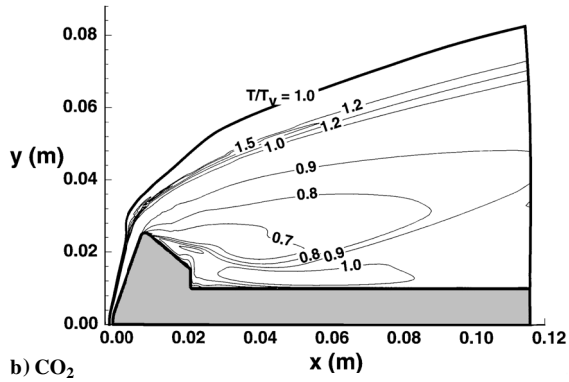

b) CO_2

Fig. 9 Ratio of translational to vibrational temperatures.

recirculation vortex formed between the free shear layer and wall remains subsonic, while the velocity within the free shear layer varies from roughly Mach 0.5 at the inner edge to Mach 2.0 at the outer edge.

The structure of the wake recirculation vortex is shown by the streamline plots in Fig. 10a for air and in Fig. 10b for CO_2. For both cases, the wake vortex extended approximately $1\frac{1}{2}$ forebody radii downstream from the base of the model. Smaller, counter-rotating vortices were also formed on the afterbody of the vehicle and at the point where the sting meets the base of the vehicle. Although the possibility of unsteady behavior of the wake has been raised by some researchers,[9–10] no evidence of any unsteadiness was observed in these computations, which is consistent with the bulk of the research on this subject.[4–8,11–14]

The breakdown of the continuum flow model in blunt-body wake flows is an issue of concern in low-density flows such as those in Refs. 10–14. However, freestream densities for the current study were much higher than for those low-density studies, and the resulting wake flowfields remained within the continuum regime. The degree of rarefaction in the flow was evaluated using the local Knudsen number, which is given by

$$Kn = (\lambda_{\mathrm{MFP}}/\rho)|\nabla\rho|$$

As discussed in Ref. 24, the use of the Navier–Stokes equations for continuum computations begins to introduce significant errors for local Knudsen numbers above 0.1, and 0.2 is the upper limit on the use of the Navier–Stokes equations. As shown in Fig. 11 for the CO_2 case (the air results are nearly identical), local Knudsen numbers remained well below the 0.2 limit throughout the wake. Local Knudsen numbers reached 0.05 in a small region near the wall around the boundary-layer separation point after the forebody corner and attained a maximum value of 0.1 only within a smaller region that cannot even be seen in Fig. 11 inside of the $Kn = 0.05$ contour. It was therefore concluded that the wake flow remained within the realm of applicability of the Navier–Stokes equations.

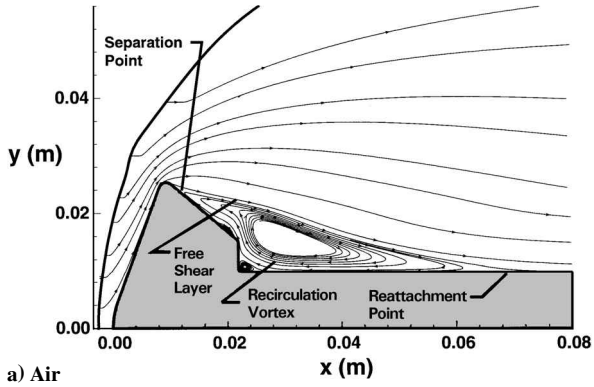

a) Air

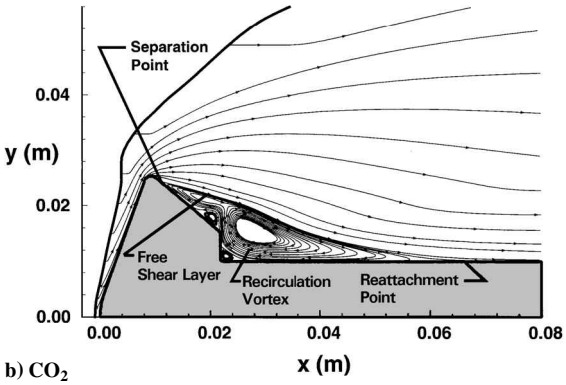

b) CO_2

Fig. 10 Near-wake streamlines.

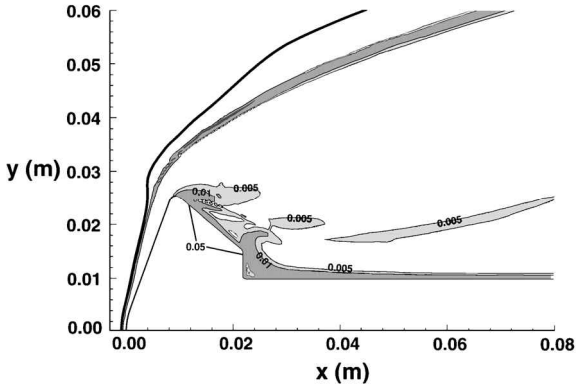

Fig. 11 Local Knudsen number contours for CO_2.

Comparison with Experiment

In Figs. 12a and 12b, heating distributions computed on the (125×180) point grids are compared with the averaged values from the experimental data presented in Part 1 (Ref. 15). Note that these forebody and wake heating distributions are plotted on separate linear scales to clearly show the details of the comparisons in both regions and that these are dimensional, not normalized, comparisons. Error bars on the experimental data represent the uncertainty estimates from Part 1 of $\pm 11\%$ for the forebody and $\pm 17\%$ for the wake at the CO_2 test condition, and $\pm 12\%$ for the forebody and $\pm 22\%$ for the wake at the air test condition. Computed forebody heating rates were within the uncertainty bounds of the experimental data for CO_2 as well as for air, except around the stagnation point. The small discrepancy here for the air case is attributed to the effects of the eigenvalue limiters on the computation. The computed wake heating rates for the air case were at least 20–30% lower than the experimental data around the free-shear-layer reattachment point, but were within the uncertainty bounds on the afterbody and on the sting outside of the reattachment region. This discrepancy is again attributed to the eigenvalue limiters. For the CO_2 case, the comparison for the wake was within the experimental uncertainty bounds

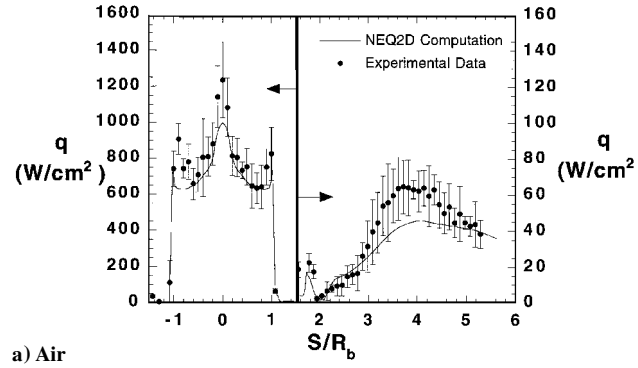

a) Air

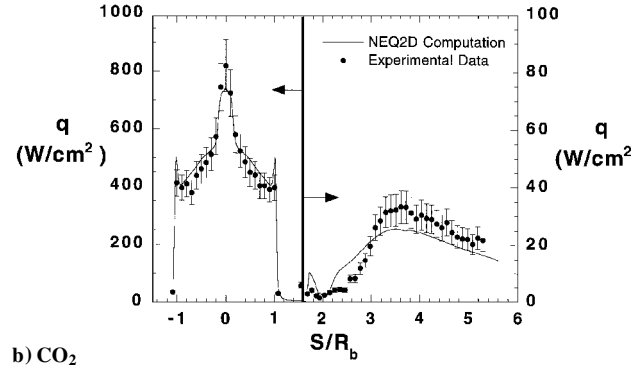

b) CO_2

Fig. 12 Comparison of computational and experimental heating data.

around the reattachment point and farther downstream on the sting, although computed wake heating rates within the recirculation vortex were overpredicted by more than 20%. This overprediction is attributed to the lack of grid resolution within this area.

Note that the effects of grid adaptation and grid resolution were both favorable in terms of comparisons with the experimental data. Adaptation and refinement moved the peak heating points further downstream, which brought them into better agreement with the experimentally determined locations. The adaptation also lowered the heating rates in the recirculation zone, which made the comparisons with experimental data in this region more favorable. Better agreement within the wake vortex could probably be obtained if the grid adaptation techniques were refined further or if greater computational resources were devoted to obtaining solutions on higher-resolution grids.

Summary and Conclusions

Numerical solutions for the forebody and wake flow around a Mars entry vehicle in both CO_2 and air were computed using a laminar, nonequilibrium Navier–Stokes solver. The freestream conditions for these computations were equivalent to those at which tests were conducted in a high-enthalpy, hypervelocity impulse facility. Through a grid-resolution/grid-adaptation study, it was demonstrated that the wake solutions were more sensitive to grid resolution than the forebody solutions, and that adaptation of the wake grid to the free shear layer produced significant changes in the solution. Comparisons between computed nondimensionalized surface pressure and heating distributions for the two cases were similar, although the higher shock density ratio in the CO_2 case produced results closer to ideal Newtonian theory predictions. Flowfield solutions showed that expansion of the flow around the forebody corner produced vibrationally and chemically frozen flow. However, as shown by computations of the local Knudsen number, the expansion was not great enough to cause noncontinuum flow behavior in the wake. A steady, recirculating flow vortex and two smaller counterrotating vortices were formed in the wake for both cases.

Comparisons were made between computational and experimental surface heat transfer distributions. For the air case, the comparisons were within the estimated experimental uncertainty both on the forebody and in the wake, except around the stagnation point at

the nose of the vehicle and the stagnation point of the free-shear-layer reattachment on the sting. The differences in these regions were attributed to the effects of the eigenvalue limiter on the computed solutions. Comparisons for the CO_2 case were within the experimental uncertainty except on the sting within the recirculation vortex, where it was concluded that higher grid resolution was required.

Acknowledgments

This research was conducted under NASA Grants NAGW-1331 and NAG1-1663 to North Carolina State University. Computer time on the NASA Langley Research Center Cray Y-MP was provided by the Aerothermodynamics Branch, NASA Langley Research Center. The authors wish to thank Graham Candler of the University of Minnesota for the use of the NEQ2D code and Stephen Alter of Lockheed Martin for the use of the VGM code.

References

[1]Bourke, R. D., Golombek, M. P., Spear, A. J., and Sturms, F. M., "MESUR and Its Role in an Evolutionary Mars Exploration Program," International Astronautical Federation, IAF Paper 92-0509, Paris, Sept. 1992.

[2]Wercinski, P. F., "Mars Aerocapture Analysis for the MESUR/Mars-Pathfinder Aeroshell in Low L/D Configurations," AIAA Paper 95-3495, Aug. 1995.

[3]Hollis, B. R., and Perkins, J. N., "High-Enthalpy and Perfect-Gas Heating Measurements on a Blunt Cone," *Journal of Spacecraft and Rockets,* Vol. 33, No. 5, 1996, pp. 628–635.

[4]Hollis, B. R., "Experimental and Computational Aerothermodynamics of a Mars Entry Vehicle," Ph.D. Dissertation, Dept. of Mechanical and Aerospace Engineering, North Carolina State Univ., Raleigh, NC, Dec. 1996; also NASA CR 201633, Dec. 1996.

[5]Horvath, T. J., McGinley, C. B., and Hannemann, K., "Blunt Body Near Wake Flow Field at Mach 6," AIAA Paper 96-1935, June 1996.

[6]Horvath, T. J., and Hannemann, K., "Blunt Body Near Wake Flow Field at Mach 10," AIAA Paper 97-0986, Jan. 1997.

[7]Kastell, D., Horvath, T. J., and Eitelberg, G., "Nonequilibrium Flow Expansion Around a Blunted Cone," 2nd European Symposium on Aerothermodynamics, European Space Research and Technology Centre (ESTEC), Noordwijk, The Netherlands, Nov. 1994.

[8]Mitchletree, R. A., and Gnoffo, P. A., "Wake Flow About a MESUR Mars Entry Vehicle," AIAA Paper 94-1958, June 1994.

[9]Haas, B. L., and Venkatapathy, E., "Mars Pathfinder Computations Including Base-Heating Predictions," AIAA Paper 95-2086, June 1995.

[10]Gochberg, L. A., Allen, G. A., Gallis, M. A., and Deiwert, G. S., "Comparison of Computations and Experiments for Nonequilibrium Flow Expansions Around a Blunted Cone," AIAA Paper 96-0231, Jan. 1996.

[11]Allegre, J., and Bisch, D., "Blunted Cone at Rarefied Hypersonic Conditions. Experimental Density Flow Fields, Heating Rates and Aerodynamic Forces," Centre National de la Recherche Scientifique, CNRS, Rept. RC 95-2, Meudon, France, Sept. 1995.

[12]Holden, M., Kolly, J., and Chadwick, K., "Calibration, Validation and Evaluation Studies in the LENS Facility," AIAA Paper 95-0291, Jan. 1995.

[13]Holden, M., Harvey, J., Boyd, I., George, J., and Horvath, T., "Experimental and Computational Studies of the Flow over a Sting Mounted Planetary Probe," AIAA Paper 97-0768, Jan. 1997.

[14]Moss, J. N., Price, J. M., Dogra, V. K., and Hash, D. B., "Comparison of DSMC and Experimental Results for Hypersonic External Flows," AIAA Paper 95-2028, June 1995.

[15]Hollis, B. R., and Perkins, J. N., "High-Enthalpy Aerothermodynamics of a Mars Entry Vehicle Part 1: Experimental Results," *Journal of Spacecraft and Rockets*, Vol. 34, No. 4, 1997, pp. 449–456.

[16]Lee, J. H., "Basic Governing Equations for the Flight Regimes of Aeroassisted Orbital Transfer Vehicles," *Thermal Design of Aeroassisted Orbital Transfer Vehicles,* edited by H. F. Nelson, Vol. 96, Progress in Aeronautics and Astronautics, AIAA, New York, 1985, pp. 3–53.

[17]Candler, G. V., and MacCormack, R. W., "Computation of Weakly Ionized Flows in Thermochemical Nonequilibrium," *Journal of Thermophysics and Heat Transfer*, Vol. 5, No. 3, pp. 226–273, 1991.

[18]Candler, G. V., and MacCormack, R. W., "The Solution of the Navier–Stokes Equations Using Gauss–Seidel Line Relaxation," *Computers and Fluids*, Vol. 17, No. 1, 1989, pp. 135–150.

[19]Park, C., "Assessment of the Two-Temperature Kinetic Model for Ionizing Air," AIAA Paper 87-1574, June 1987.

[20]Candler, G. V., "Computation of Thermo-Chemical Nonequilibrium Martian Atmospheric Entry Flows," AIAA Paper 90-1695, June 1990.

[21]Gnoffo, P. A., Hartung, L. C., and Greendyke, R. B., "Heating Analysis for a Lunar Transfer Vehicle at Near-Equilibrium Conditions," AIAA Paper 93-0270, Jan. 1993.

[22]Alter, S. A., "The Volume Grid Manipulator (VGM): A Grid Reusability Tool," NASA CR 4772, April 1997.

[23]Lees, L., "Hypersonic Wakes and Trails," *AIAA Journal,* Vol. 2, No. 3, 1964, pp. 417–428.

[24]Bird, G. A., *Molecular Gas Dynamics and the Direct Simulation of Gas Flows,* Clarendon, Oxford, England, UK, 1994.

B. A. Bhutta
Associate Editor